ACS APPLIED MATERIALS & INTERFACES

Research Article

www.acsami.org

Hierarchical Assembly of α-Fe_2O_3 Nanosheets on SnO_2 Hollow Nanospheres with Enhanced Ethanol Sensing Properties

Peng Sun,* Chen Wang, Jiangyang Liu, Xin Zhou, Xiaowei Li, Xiaolong Hu, and Geyu Lu*

State Key Laboratory on Integrated Optoelectronics, College of Electronic Science and Engineering, Jilin University, Changchun 130012, People's Republic of China

Supporting Information

ABSTRACT: We present the preparation of a hierarchical nanoheterostructure consisting of inner SnO_2 hollow spheres (SHS) surrounded by an outer α-Fe_2O_3 nanosheet (FNS). Deposition of the FNS on the SHS outer surface was achieved by a facile microwave hydrothermal reaction to generate a double-shell SHS@FNS nanostructure. Such a composite with novel heterostructure acted as a sensing material for gas sensors. Significantly, the hierarchical composites exhibit excellent sensing performance toward ethanol, which is superior to the single component (SHS), mainly because of the synergistic effect and heterojunction.

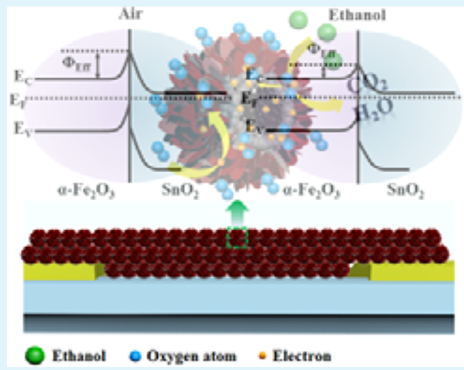

KEYWORDS: *microwave hydrothermal method, semiconductor, hollow nanostructure, α-Fe_2O_3/SnO_2 composites, gas sensor*

1. INTRODUCTION

Gas sensors have been acknowledged as profilers to detect and quantify inflammable, explosive, or toxic gases.[1−4] For the design and fabrication of high performance gas sensors in terms of sensitivity, selectivity, and stability, understanding the properties of the sensing material that affect sensor performance is of great necessary. Therefore, the development of highly efficient sensitive materials is one of the most important topics in gas sensor research. In general, ideal sensing materials for gas sensors should be cheap, nontoxic, and stable. Considering their advantages of high sensitivity and simplicity in synthesis, semiconductor oxides, including α-Fe_2O_3, SnO_2, ZnO, and In_2O_3, have been increasingly researched as sensing materials over the past few decades.[5−9] The sensing mechanism of sensors employing semiconductor oxides is mainly that the adsorption and reaction of oxygen and target gases result in a change in the electrical conductivity.[10−13] Thus, the morphology, microstructure, composition, and crystalline size play an important role in their gas sensing properties. The sensitivity of the sensor increases significantly when the size of the sensing materials decrease to be a similar thickness as that of the electron depletion layer.[14] Many satisfactory results regarding sensing properties of semiconductor oxides have been obtained, but the design and development of highly sensitive and selective sensing materials remains a challenge for gas sensors. Indeed, during the past decade, many efforts have been dedicated to modifying semiconductor oxide sensing materials, including the modulation of surface states by doping with elements,[15−17] the construction of heterojunctions by combining them with different semiconductor oxides,[18−20] and the addition of catalysts on the surface of the semiconductor oxides.[21−23] Recently, much research has been carried out aiming to enhance the performance of gas sensors by applying heterostructure semiconductor composites.[24−26] Because the sensing properties of heterostructure composites are strongly related to their morphologies, preparation of composites with unique architectures will be increasingly important for constructing high performance gas sensors.

SnO_2 and α-Fe_2O_3, two of the important n-type semiconductors, have received widespread attention because of their unique characters and vast potential applications in various fields.[27−31] It has been previously demonstrated that an α-Fe_2O_3/SnO_2 hybrid composite can yield enhanced functions, such as gas response, photocatalyst, and lithium storage capacity.[32−37] Therefore, hierarchical α-Fe_2O_3/SnO_2 composites with various architectures have been prepared through different strategies. Solution-phase synthesis methods have been demonstrated to be a versatile and efficient route to finely adjust semiconductor composites with different compositions and microstructures.[38−40] However, despite the exciting results that have been obtained, there are few reports on the hierarchical double-shell α-Fe_2O_3/SnO_2 nanostructures consisting of inner SnO_2 hollow nanospheres surrounded by outer α-Fe_2O_3 nanosheets. In this work, we successfully prepared hollow α-Fe_2O_3/SnO_2 composites by combining a hydrothermal route (for the hollow SnO_2 nanosphere) and a

Received: May 30, 2015
Accepted: August 18, 2015
Published: August 18, 2015

DOI: 10.1021/acsami.5b04751
ACS Appl. Mater. Interfaces 2015, 7, 19119−19125

microwave-assisted hydrolytic reaction (for the α-Fe_2O_3 nanosheets). Moreover, such novel α-Fe_2O_3/SnO_2 heterostructures as sensing materials have been demonstrated, and they displayed that the α-Fe_2O_3/SnO_2 composites had superior sensing performance to that of the SnO_2 individual component in terms of high gas response to ethanol. The variation of the heterojunction barrier at the diverse gas ambience and the synergistic effect of α-Fe_2O_3 and SnO_2 were suggested to be the origin of the enhanced performance.

2. EXPERIMENTAL SECTION

Preparation of Hollow α-Fe_2O_3/SnO_2 Hierarchical Composites. SnO_2 hollow nanospheres were obtained as described in our previous publication.[19] The α-Fe_2O_3/SnO_2 semiconductor heterostructures were synthesized through a microwave-assisted hydrothermal reaction without any surfactant. Briefly, 0.03 g of the as-prepared hollow SnO_2 spheres were added to a mixed solvent of 5 mL of glycerol and 35 mL of deionized water with vigorous stirring. Then, 0.79 g of $FeCl_2{\cdot}4H_2O$ and 0.69 g of K_2SO_4 were dissolved into the mixed solution, respectively. Then, the above suspension was poured into a Teflon-lined autoclave and heated with a predetermined heating procedure (first heated to 180 °C from 25 °C, then kept at 180 °C for 2 h, and afterwards cooled naturally) in a microwave hydrothermal apparatus. The resulting product was centrifuged and washed with deionized water and ethanol several times and finally dried at 80 °C.

Characterization. The phase structures of the as-obtained samples were characterized through X-ray powder diffraction on a Rigaku TTRIII X-ray diffractometer, and the data were recorded from 20° to 70°. The morphologies and microstructures were investigated by field-emission scanning electron microscopy (FESEM) using a JEOL JSM-7500F microscope. Transmission electron microscopy (TEM) images and the energy dispersive X-ray spectrometry (EDS) pattern were obtained by a JEOL JEM-3010 microscope and its attachment, respectively. Specific surface areas of the samples were calculated by the Brunauer−Emmett−Teller (BET) equation according to the N_2 adsorption/desorption isotherm recorded using Micromeritics Gemini VII equipment (Surface Area and Porosity System).

Fabrication and Measurement of Gas Sensors. For gas response, the obtained products were coated onto the surface of a commercially produced ceramic tube to form a thick sensing film. The as-fabricated devices were fired to 400 °C for 2 h in air using a muffle furnace. A Ni−Cr alloy coil, as a heater, was threaded to the ceramic tube to regulate the entire operating temperature of the sensor. The details of the fabrication and measurement process of the gas sensor are described in our previous works.[15,23] A static system was applied to investigate the gas sensing performances of the sensors under laboratory conditions (40% RH, 23 °C). The response of the sensor was measured as the resistance ratio between the air (R_a) and the target gas (R_g). The time consumed by the sensor to reach 90% of the total resistance change in tested gas and air were defined as the response time and recovery time, respectively.

3. RESULTS AND DISCUSSION

Structural and Morphological Characteristics. The XRD pattern in Figure 1 displays the phase purity and crystallographic structure of the as-prepared hierarchical α-Fe_2O_3/SnO_2 nanostructures. All the diffraction peaks in this XRD pattern for the composite contained a tetragonal rutile structure of SnO_2 and rhombohedral structure of α-Fe_2O_3, which were accorded well with those from the standard Joint Committee on Powder Diffraction Standards (JCPDS) card of SnO_2, No. 41-1445, with a = 0.4738 nm and c = 0.3187 nm and the JCPDS card of α-Fe_2O_3, No. 33-0664, with a = 0.5035 nm and c = 1.375 nm, respectively. Moreover, no other diffraction peaks derived from impurities were found, indicating high purity of the as-prepared product.

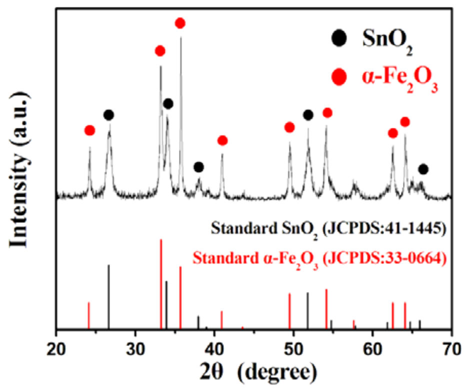

Figure 1. XRD pattern of the hierarchical α-Fe_2O_3/SnO_2 composites.

The images in Figure 2 present the morphologies and microstructures of the as-obtained samples: hollow SnO_2 nanospheres and hierarchical α-Fe_2O_3/SnO_2 nanostructures. Figure 2a depicts a low-magnification FESEM image of the SnO_2 sample fabricated through the first hydrothermal route using SnC_2O_4 as the precursor. It is apparent that the product consisted of monodisperse spheres that were ∼400 nm in diameter. No other morphologies could be observed, which indicated that good uniformity and dispersibility were achieved through this strategy. The enlarged FESEM image in Figure 2b provides a single SnO_2 sphere; it is found that the SnO_2 sphere consisted of many primary particles with a size of a few dozen nanometers. From a broken nanosphere, as shown in Figure 2c, the hollow structure and the nanometer-scale primary particles could be clearly identified. Moreover, the thickness of spherical shell was ∼100 nm. TEM images further reveal the hollow interior of the SnO_2 spheres. As can be seen in Figure 2d, the contrasting light and dark between the center and the edge of the spheres confirmed that these spheres possessed a hollow interior. Figure S1 displays a high-resolution TEM (HRTEM) image of nanoparticles on the surface of the sphere where the (110) lattice spacing of ∼0.335 nm of tetragonal rutile SnO_2 could be clearly observed.[41] After the second solution growth, the product exhibited hierarchical α-Fe_2O_3/SnO_2 hollow nanostructures. A panoramic view of the composites, as

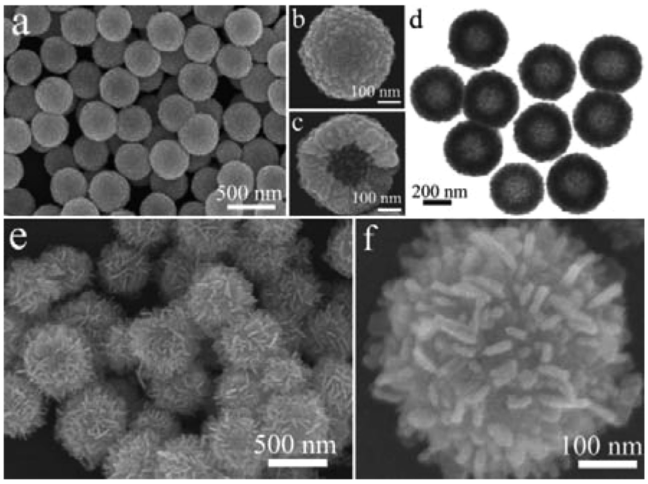

Figure 2. (a−d) Typical FESEM and TEM images of SnO_2 spheres. (e and f) FESEM images of the as-synthesized hierarchical α-Fe_2O_3/SnO_2 composites.

DOI: 10.1021/acsami.5b04751
ACS Appl. Mater. Interfaces 2015, 7, 19119−19125

shown in Figure 2e, reveals that they were composed of very uniform spherical particles with diameters of ~600 nm. The high-magnification FESEM presented in Figure 2f displays the detailed morphological information on a single hierarchical sphere. It is found that the α-Fe_2O_3 nanosheets, with an average thickness of ~10 nm, assembled hierarchically on the surface of hollow SnO_2 nanospheres.

Such hierarchical composites were analyzed by TEM to get deeper insight into their structure, images of which are displayed in Figure 3. An obviously hollow interior could be

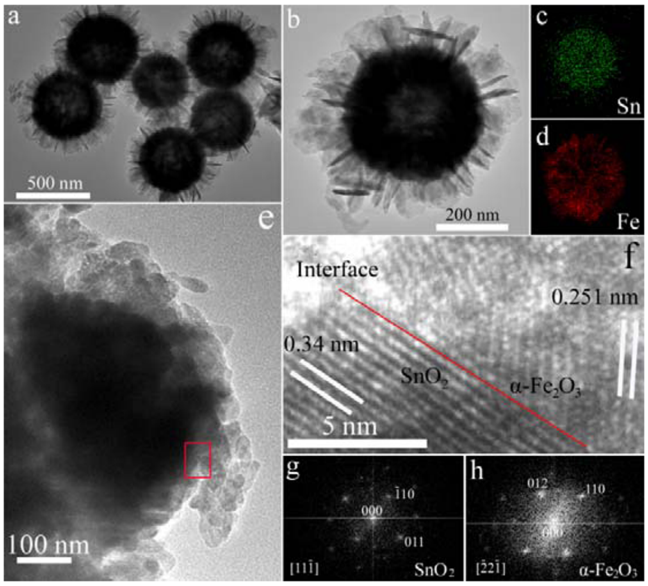

Figure 3. (a, b, and e) Typical TEM images of as-obtained hierarchical α-Fe_2O_3/SnO_2 composites. (c and d) Elemental mapping images. (f) HRTEM images of the interfacial region if ab α-Fe_2O_3/SnO_2 hollow nanosphere. (g and h) FFT patterns taken from SnO_2 and α-Fe_2O_3, respectively.

clearly observed from a low magnification TEM image (Figure 3a). Careful observation of a single sphere (Figure 3b) indicates that the hollow sphere had an obvious double-shell structure. The inner shell could be identified as a hollow SnO_2 sphere, which appeared black colored in the image due to high mass–thickness contrast. The outer shell of the hierarchical sphere was composed of numerous α-Fe_2O_3 nanosheets. The thickness of the α-Fe_2O_3 shell was observed to be ~100 nm by measuring the light-colored region in the image. The TEM elemental mapping taken from a single hierarchical sphere (Figure 3b) clearly identified the spatial distributions of Sn and Fe elements in the composite, as shown in Figure 3c and d. The signal of Sn was strongly detected in the inner shell region of the hollow sphere, whereas the Fe element was mainly distributed in the outer shell region. A typical HRTEM image of the interfacial region in α-Fe_2O_3/SnO_2 hollow nanospheres (outlined by a red box in Figure 3e) is presented in Figure 3f, which indicated that there was good lattice compatibility at the interface. The fringe spacings were approximately 0.34 and 0.251 nm, which corresponded to the (110) plane of SnO_2 and the (110) plane of α-Fe_2O_3, respectively.[30,41] The fast-Fourier transform (FFT) patterns selected from SnO_2 and α-Fe_2O_3 are displayed in Figure 3g and h, respectively. The α-Fe_2O_3 nanosheet gave the (012) plane to constitute the interface with the (110) plane of SnO_2.[33]

The formation mechanism of the α-Fe_2O_3/SnO_2 heterostructure composite was investigated through a series of experiments. The FESEM images in Figure 4a–d show the

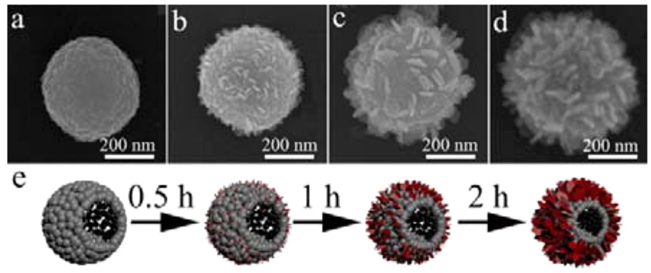

Figure 4. (a–d) FESEM images of the samples at various reaction times: (a) 0 h, (b) 0.5 h, (c) 1 h, and (d) 2 h. (e) Schematic of the growth process of the α-Fe_2O_3/SnO_2 composite.

samples prepared at different reaction times, which reveal the morphological and structural changes from SnO_2 hollow spheres to α-Fe_2O_3/SnO_2 double-shell structural composites. During the initial 30 min reaction, small nanosheets of ~8 nm thickness were found to be growing on the surfaces of the SnO_2 hollow spheres (Figure 4b). With an extended reaction time, the size, thickness, and quantity of nanosheets increased, and the product exhibited a flower-like morphology (Figure 4c and d). On the basis of the above observations, a process of forming the hierarchical α-Fe_2O_3/SnO_2 double-shell hollow spheres during the microwave hydrothermal reaction is proposed and is presented schematically in Figure 4e. At first, the hydrolysis of $FeCl_2 \cdot 4H_2O$ will lead to the formation of iron oxide nanoparticles; then, these nanoparticles will aggregate on the surface of SnO_2 spheres. During the extended microwave hydrothermal reaction, the as-obtained nanoparticles will grow into flaky nanostructures, forming rough shells, which result in the obtention of a double-shell hollow structure. The specific growth mechanism of the unique double-shell heterostructures is still under investigation. Presented here is just an assumption that corresponds well with the results from electron microscopy.

The specific surface areas of hollow SnO_2 and α-Fe_2O_3/SnO_2 spheres were estimated through the data of N_2 adsorption/desorption isotherms by the BET method, as shown in Figure 5. For two structures, an obvious hysteresis loop was observed from the nitrogen adsorption isotherm, which indicated mesoporous structures in hollow spheres.[42] From the corresponding pore size distribution curves (insets in Figure 5), the distribution centers had almost no change. Moreover, as found by the results of the BET measurements, such a hierarchical α-Fe_2O_3/SnO_2 heterostructure composite gave a slightly larger specific surface area (26.1 $m^2\ g^{-1}$) and total pore volume (0.13 $cm^3\ g^{-1}$) relative to those of the hollow SnO_2 spheres (22.9 $m^2\ g^{-1}$, 0.07 $cm^3\ g^{-1}$, respectively). The relatively high pore volume in the double shell α-Fe_2O_3/SnO_2 hollow spheres seems to afford an efficient way to transmit to their interior space, which is critical for gas sensoring and other applications.

Sensing Properties. Recently, vast efforts have been spent searching for excellent sensing materials to enhance the performance of gas sensors. Here, we employed the prepared hierarchical α-Fe_2O_3/SnO_2 nanostructures as a potential sensing material for gas sensors as compared with the pristine SnO_2 hollow nanospheres. For semiconductor oxide gas

DOI: 10.1021/acsami.5b04751
ACS Appl. Mater. Interfaces 2015, 7, 19119–19125

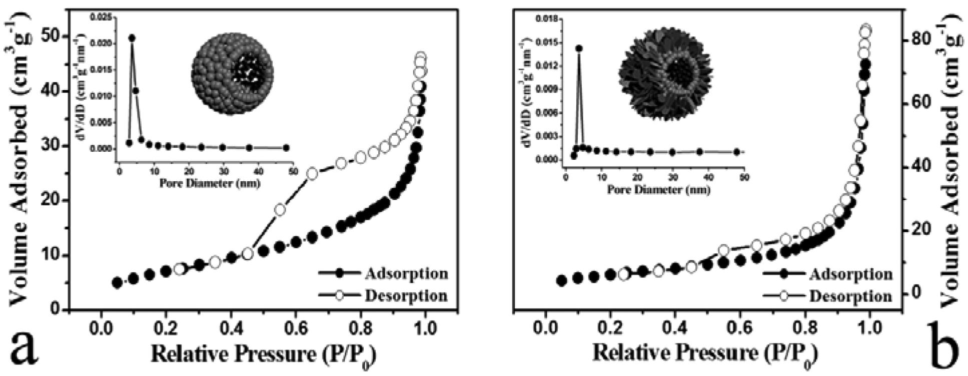

Figure 5. Typical N_2 adsorption/desorption isotherms and pore size distribution curves of (a) SnO_2 hollow nanospheres and (b) hierarchical α-Fe_2O_3/SnO_2 composites.

sensors, the operating temperature plays an important role in their response to target gas.[10] Therefore, the responses of the two sensors to 100 ppm of C_2H_5OH were measured as a function of operating temperature to ascertain the optimum operating temperature of the sensors, as shown in Figure 6a. From which a volcano-like correlation between response and operating temperature is observed. In other words, the responses of the tested sensors increased first and then decreased with increasing temperature. The response showed a maximum value of 18.4 for the hierarchical α-Fe_2O_3/SnO_2 composites and 9.5 for the hollow SnO_2 nanospheres at 225 °C, which was therefore chosen for the two gas sensors as the optimal operating temperature. The results indicate that the hierarchical composites displayed a remarkably improved gas response (18.4), which was almost twice that of the SnO_2 hollow spheres (9.5).

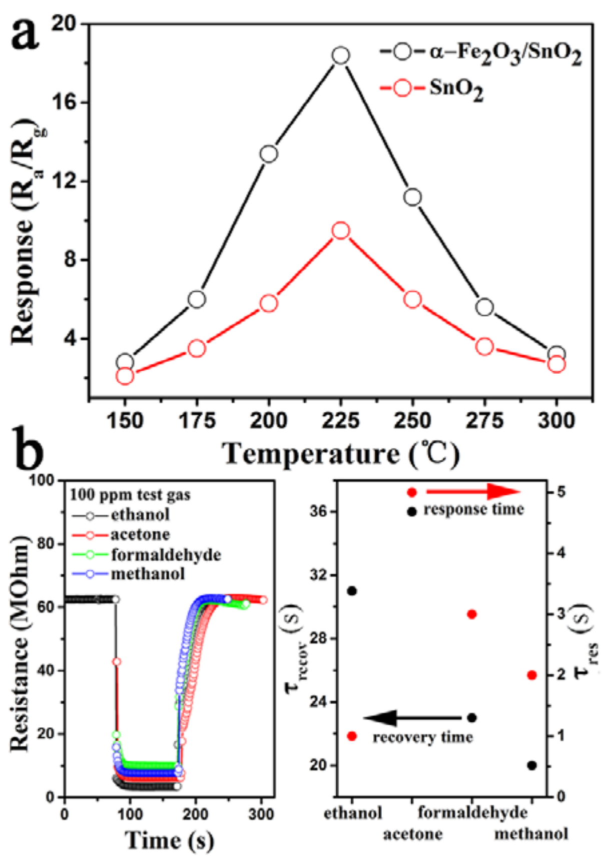

Figure 6. (a) Response of pristine SnO_2 hollow nanospheres and α-Fe_2O_3/SnO_2 hierarchical composites relative to operating temperature to 100 ppm of C_2H_5OH. (b) Response transients of hollow α-Fe_2O_3/SnO_2 double-shell heterostructures to 100 ppm of C_2H_5OH, C_3H_6O, HCHO, and CH_3OH at 225 °C.

The dynamic response characteristics of the α-Fe_2O_3/SnO_2 sensor to diverse reducing gases were then studied. Figure 6b presents the response of hollow heterostructures to 100 ppm of C_2H_5OH, C_3H_6O, HCHO, and CH_3OH for a cycle period at 225 °C. It is found that the sensor showed an n-type response to tested gases and exhibited a sensitive and reversible response. Obviously, with the introduction of tested gases, the sensor responded immediately and the resistance reached a near steady state within seconds.[43] Because the tested gas further diffused through the sensing layer and occupied the residual surface reaction sites, the resistance then changed slowly. When the sensor was placed in air, the resistance gragually increased and finally returned to almost its baseline level. The response was 18.4, 10.1, 6.3, and 8.1 for 100 ppm of C_2H_5OH, C_3H_6O, HCHO, and CH_3OH, respectively. The reproducibility of the sensor upon 8 cycle response measurements to 60 ppm ethanol at 225 °C (Figure S2) revealed there was no evident change in the response amplitude, which indicated that the sensor had good reproducibility. Moreover, among these tested gases, the sensor showed the maximum response to ethanol. The response time of the sensor was 1, 5, 3, and 2 s for ethanol, acetone, formaldehyde, and methanol, respectively. After exposure in air, the recovery time of the sensor was 31, 36, 23, and 20 s for ethanol, acetone, formaldehyde, and methanol, respectively.

The relationships between the responses and ethanol concentrations for the two sensors at 225 °C is depicted in Figure 7a. From the curves, it can be seen that the responses of the sensors were proportional to the increasing concentrations of ethanol from 10 to 100 ppm. However, the sensor, using hierarchical composites, by contrast, exhibited a high response to each concentration of ethanol. Moreover, the response of the α-Fe_2O_3/SnO_2 composites tended to rise faster than that of the hollow SnO_2 spheres with increasing C_2H_5OH concentration. Panels b and c in Figure 7 demonstrate the dynamic resistance changes of the two sensors to various concentrations of ethanol at 225 °C. Obviously, the response and recovery characteristics of the sensors were nearly reproducible with the rapid response and recovery. The response of the sensor using heterostructure α-Fe_2O_3/SnO_2 hierarchical composites was approximately 2.4, 4.1, 6.3, 9.9, 13.3, and 18.4 to 10, 20, 40, 60, 80, and 100 ppm of C_2H_5OH, respectively, whereas the response of pure SnO_2

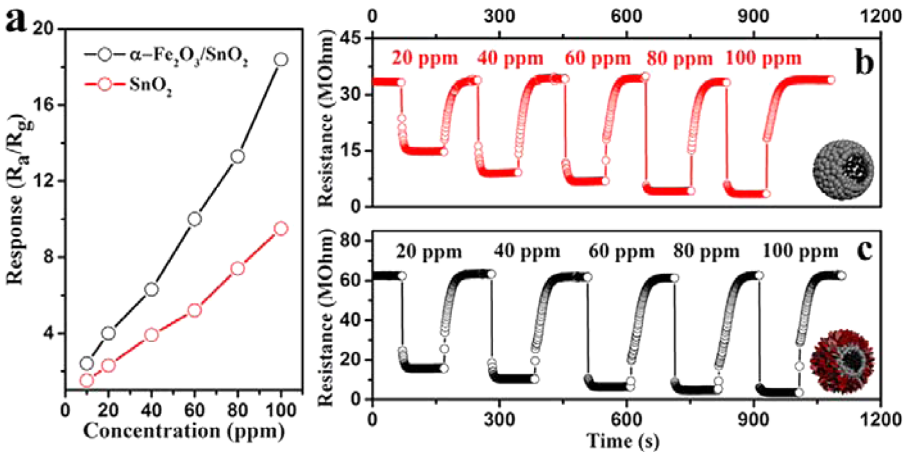

Figure 7. (a) Responses of the two sensors relative to C_2H_5OH concentrations at 225 °C. (b and c) Response transients of hollow SnO_2 nanospheres and hierarchical α-Fe_2O_3/SnO_2 heterostructures to diverse concentrations of ethanol at 225 °C.

was 1.5, 2.3, 3.9, 5.2, 7.4, and 9.5 for each respective concentration.

In terms of practical applications, the long-term stability of the sensor is considered an important parameter. Therefore, successive tests of the response toward 60 ppm ethanol for the sensor using the as-obtained hierarchical α-Fe_2O_3/SnO_2 heterostructures at 225 °C were carried out, as shown in Figure 8a. It is found that the sensor maintained its initial

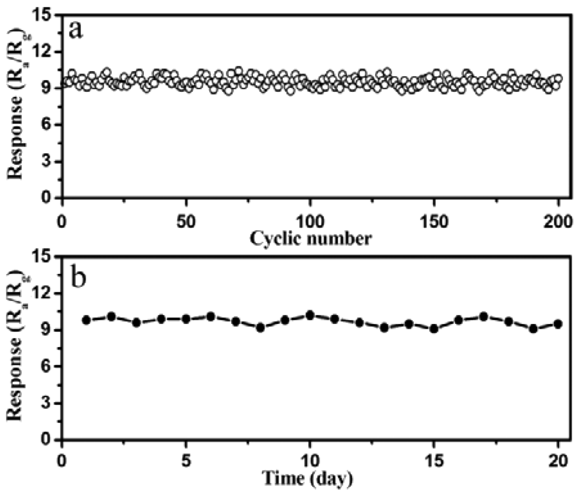

Figure 8. Response of hierarchical α-Fe_2O_3/SnO_2 hollow heterostructures as a function of the number of (a) cyclic measurements and (b) tested days to 60 ppm of ethanol at 225 °C.

response after 200 cyclic tests, which indicated that the hierarchical composites had excellent repeatability. Moreover, the repeated tests were conducted every day, which revealed that the responses were almost constant without an obvious increase/decrease even after 20 days, as shown in Figure 8b. The result further confirmed that the present sensor might have a practical application on the basis of its good stability.

The enhanced performance is more likely derived from the novel heterostructure of the as-synthesized composite rather than simply a result of the addition of the other sensing component, which is described as follows. On one hand, the improved response of hierarchical composites compared with the primary SnO_2 hollow nanospheres can be easily understood by the synergistic effect of α-Fe_2O_3 and SnO_2. It has been reported that the surface reactions between tested gases and adsorbed oxygen species depend on the acid−base properties of oxide semiconductors. In terms of ethanol gas, the base property will be beneficial for the reaction with adsorbed oxygen.[44−48] In this work, the addition of α-Fe_2O_3 enhances the basicity of the composite because α-Fe_2O_3 and SnO_2 are basic oxides. Therefore, the heterostructure of the composites exhibits a higher response to ethanol than that of pristine SnO_2. On the other hand, the band configuration at the interface of the α-Fe_2O_3/SnO_2 composites in different atmospheres is proposed, as shown in Scheme 1, where Φ_{eff}

Scheme 1. Schematic Diagram of Band Configuration at the Interface of the α-Fe_2O_3/SnO_2 Nanoheterostructure in Different Atmospheres

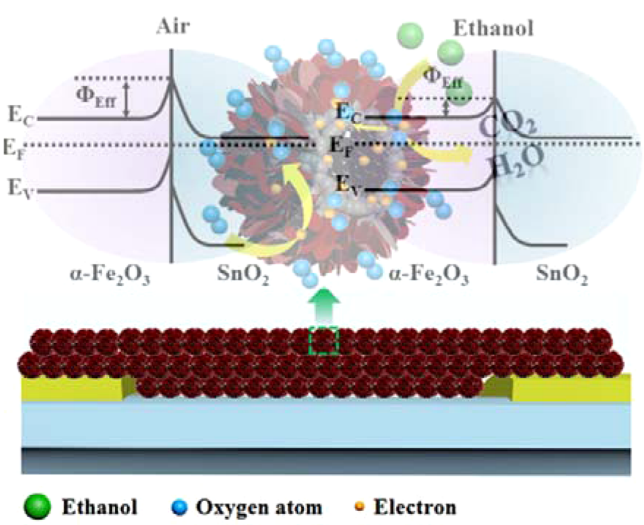

is the effective barrier height.[49] For composites, electron transport will be strongly modulated by the heterojunction barrier, which has been generally researched for many heterostructures of devices.[50−53] It has been clarified that the conductivity of the heterostructures of the composites is inversely proportional to the barrier height at the high temperature.[49] When the composites are exposed to air, the electrons in conduction bands of α-Fe_2O_3 and SnO_2 are trapped by oxygen to form adsorbed oxygen species, which results in the increase of the barrier height (Scheme 1), thereby

DOI: 10.1021/acsami.5b04751
ACS Appl. Mater. Interfaces 2015, 7, 19119−19125

decreasing the conductivity owing to the lower free electron concentration upon exposure to a given reducing gas, such as C_2H_5OH, which will react with oxygen species. As a result, the electrons trapped in the adsorbed oxygen species are released back into the conduction bands of α-Fe_2O_3 and SnO_2.[54,55] As such, the barrier height will be decreased due to the higher concentration of electrons. Therefore, the resistance of the heterostructures is greatly decreased. This means that the response of hierarchical composites to ethanol can be enhanced. Thus, the synergistic effect and the change of barrier height in the diverse gas atmosphere may be the origin of the improvement in gas sensing performance.

4. CONCLUSIONS

In summary, a novel hierarchical α-Fe_2O_3/SnO_2 nanoheterostructure has been prepared by a facile solution strategy. The uniqueness of the structure is that α-Fe_2O_3 nanosheets are hierarchically assembled onto the surface of SnO_2 hollow nanospheres. The as-obtained α-Fe_2O_3/SnO_2 composite was applied as the sensing material for the gas sensor. In comparison to a single component (SnO_2 hollow nanosphere), the composite has demonstrated superior sensing performance toward ethanol. The improvement may be ascribed to variation of the heterojunction barrier in the diverse gas atmosphere.

■ ASSOCIATED CONTENT

Supporting Information

The Supporting Information is available free of charge on the ACS Publications website at DOI: 10.1021/acsami.5b04751.

Typical TEM images of as-prepared hollow SnO_2 spheres, HRTEM images, and response transitions of the sensor using double-shell α-Fe_2O_3/SnO_2 hollow spheres to 60 ppm of ethanol (PDF)

■ AUTHOR INFORMATION

Corresponding Authors

*E-mail: spmaster2008@163.com

*Tel: +86 431 85167808. Fax: +86 431 85167808. E-mail: lugy@jlu.edu.cn.

Notes

The authors declare no competing financial interest.

■ ACKNOWLEDGMENTS

This work is supported by the National Nature Science Foundation of China (Nos. 61374218, 61134010, and 61327804), Program for Chang Jiang Scholars and Innovative Research Team in University (No. IRT13018), and National High-Tech Research and Development Program of China (863 Program, No. 2013AA030902 and 2014AA06A505).

■ ABBREVIATIONS

SHS, SnO_2 hollow spheres
FNS, α-Fe_2O_3 nanosheets
XRD, X-ray power diffraction
FESEM, field-emission scanning electron microscopy
TEM, transmission electron microscopy
HRTEM, high-resolution transmission electron microscopy
EDS, energy dispersive X-ray spectrometry
FFT, fast-Fourier transform
BET, Brunauer−Emmett−Teller

■ REFERENCES

(1) Kong, J.; Franklin, N. R.; Zhou, C.; Chapline, M. G.; Peng, S.; Cho, K.; Dai, H. Nanotube Molecular Wires as Chemical Sensors. *Science* **2000**, *287*, 622−625.

(2) Hahn, Y. B.; Ahmad, R.; Tripathy, N. Chemical and Biological Sensors Based on Metal Oxide Nanostructures. *Chem. Commun.* **2012**, *48*, 10369−10385.

(3) Cui, Y.; Wie, Q. Q.; Park, H. K.; Lieber, C. M. Nanowire Nanosensors for Highly Sensitive and Selective Detection of Biological and Chemical Species. *Science* **2001**, *293*, 1289−1292.

(4) Hagleitner, C.; Hierlemann, A.; Lauge, D.; Kimmer, A.; Kerness, N.; Brand, O.; Baltes, H. Smart Single-Chip Gas Sensor Microsystem. *Nature* **2001**, *414*, 293−296.

(5) Wang, Y. L.; Jiang, X. C.; Xia, Y. N. A Solution-Phase, Precursor Route to Polycrystalline SnO_2 Nanowires That Can Be Used for Gas Sensing Under Ambient Conditions. *J. Am. Chem. Soc.* **2003**, *125*, 16176−16177.

(6) Hernandez-Ramirez, F.; Prades, J. D.; Hackner, A.; Fischer, T.; Mueller, G.; Mathur, S.; Morante, R. Miniaturized Ionization Gas Sensors from Single Metal Oxide Nanowires. *Nanoscale* **2011**, *3*, 630−634.

(7) Vallejos, S.; Stoycheva, T.; Umek, P.; Navio, C.; Snyders, R.; Bittencourt, C.; Llobet, E.; Blackman, C.; Moniz, S.; Correig, X. Au Nanoparticle-Functionalised WO_3 Nanoneedles and Their Application in High Sensitivity Gas Sensor Devices. *Chem. Commun.* **2011**, *47*, 565−567.

(8) Waitz, T.; Wagner, T.; Sauerwald, T.; Kohl, C.-D.; Tiemann, M. Ordered Mesoporous In_2O_3: Synthesis by Structure Replication and Application as a Methane Gas Sensor. *Adv. Funct. Mater.* **2009**, *19*, 653−661.

(9) Li, J.; Fan, H. Q.; Jia, X. H. Multilayered ZnO Nanosheets with 3D Porous Architectures: Synthesis and Gas Sensing Application. *J. Phys. Chem. C* **2010**, *114*, 14684−14691.

(10) Yamazoe, N.; Sakai, G.; Shimanoe, K. Oxide Semiconductor Gas Sensor. *Catal. Surv. Asia* **2003**, *7*, 63−75.

(11) Egashira, M.; Shimizu, Y.; Takao, Y.; Sako, S. Variations in I-V Characteristics of Oxide Semiconductors Induced by Oxidizing Gases. *Sens. Actuators, B* **1996**, *35*, 62−67.

(12) Dayan, N. J.; Sainkar, S. R.; Karekar, R. N.; Aiyer, R. C. Formulation and Characterization of ZnO:Sb Thick-Film Gas Sensor. *Thin Solid Films* **1998**, *325*, 254−258.

(13) Williams, D. E. Semiconductor Oxides as Gas-Sensitive Resistors. *Sens. Actuators, B* **1999**, *57*, 1−16.

(14) Yamazoe, N. New Approaches for Improving Semiconductor Gas Sensors. *Sens. Actuators, B* **1991**, *5*, 7−19.

(15) Sun, P.; Zhou, X.; Wang, C.; Wang, B.; Xu, X. M.; Lu, G. Y. One-Step Synthesis and Gas Sensing Properties of Hierarchical Cd-Doped SnO_2 Nanostructures. *Sens. Actuators, B* **2014**, *190*, 32−39.

(16) Wang, H. K.; Dou, K. P.; Teoh, W. Y.; Zhan, Y. W.; Hung, T. F.; Zhang, F. H.; Xu, J. Q.; Zhang, R. Q.; Rogach, A. L. Engineering of Facets, Band Structure, and Gas Sensing Properties of Hierarchical Sn^{2+}-Doped SnO_2 Nanostructures. *Adv. Funct. Mater.* **2013**, *23*, 4847−4853.

(17) Han, N.; Wu, X. F.; Zhang, D. W.; Shen, G. L.; Liu, H. D.; Chen, Y. F. CdO Activated Sn-Doped ZnO for Highly Sensitive, Selective and Stable Formaldehyde Sensor. *Sens. Actuators, B* **2011**, *152*, 324−329.

(18) Shan, H.; Liu, C. B.; Liu, L.; Zhang, J. B.; Li, H. Y.; Liu, Z.; Zhang, X. B.; Bo, X. Q.; Chi, X. Excellent Toluene Sensing Properties of SnO_2-Fe_2O_3 Interconnected Nanotubes. *ACS Appl. Mater. Interfaces* **2013**, *5*, 6376−6380.

(19) Sun, P.; Zhou, X.; Wang, C.; Shimanoe, K.; Lu, G. Y.; Yamazoe, N. Hollow SnO_2/α-Fe_2O_3 Spheres with a Double-Shell Structure for Gas Sensors. *J. Mater. Chem. A* **2014**, *2*, 1302−1308.

(20) Si, S. F.; Li, C. H.; Wang, X.; Peng, Q.; Li, Y. D. Fe_2O_3/ZnO Core-Shell Nanorods for Gas Sensors. *Sens. Actuators, B* **2006**, *119*, 52−56.

(21) Lü, R. J.; Zhou, W.; Shi, K. Y.; Yang, Y.; Wang, L.; Pan, K.; Tian, C. G.; Ren, Z. Y.; Fu, H. G. Alumina Decorated TiO_2 Nanotubes with

Ordered Mesoporous Walls as High Sensitivity NO_X Gas Sensor at Room Temperature. *Nanoscale* **2013**, *5*, 8569−8576.
(22) Kolmakov, A.; Kienov, D. O.; Liach, Y.; Stemmer, S.; Moskovits, M. Enhanced Gas Sensing by Individual SnO_2 Nanowires and Nanobelts Fnctionalized with Pd Catalyst Particles. *Nano Lett.* **2005**, *5*, 667−673.
(23) Sun, P.; Yu, Y. S.; Xu, J.; Sun, Y. F.; Ma, J.; Lu, G. Y. One-Step Synthesis and Gas Sensing Characteristics of Hierarchical SnO_2 Nanorods Modified by Pd Loading. *Sens. Actuators, B* **2011**, *160*, 244−250.
(24) Chu, D. W.; Zeng, Y. P.; Jiang, D. L.; Masuda, Y. In_2O_3-SnO_2 Nano-Toasts and Nanorods: Precipitation Preparation, Formation Mechanism, and Gas Sensitive Properties. *Sens. Actuators, B* **2009**, *137*, 630−636.
(25) Yu, H. L.; Li, L.; Gao, X. M.; Zhang, Y.; Meng, F. N.; Wang, T. S.; Xiao, G.; Chen, Y. J.; Zhu, C. L. Synthesis and H_2S Gas Sensing Properties of Cage-Like MoO_3/ZnO Composite. *Sens. Actuators, B* **2012**, *171/172*, 679−685.
(26) Zhang, S. F.; Ren, Feng; Wu, Wei; Zhou, J.; Xiao, X. H.; Sun, L. J.; Liu, Y.; Jiang, C. Z. Controllable Synthesis of Recyclable Core-Shell γ-Fe_2O_3@SnO_2 Hollow Nanoparticles with Enhanced Photocatalytic and Gas Sensing Properties. *Phys. Chem. Chem. Phys.* **2013**, *15*, 8228−8236.
(27) Huang, H.; Ong, C. Y.; Guo, J.; White, T.; Tse, M. S.; Tan, O. K. Pt Surface Modification of SnO_2 Nanorod Arrays for CO and H_2 Sensors. *Nanoscale* **2010**, *2*, 1203−1207.
(28) Yao, F.; Duong, D. L.; Lim, S. L.; Yang, S. B.; Hwang, H. R.; Yu, W. J.; Günes, F.; Lee, Y. H. Humidity-Assisted Selective Reactivity Between NO_2 and SO_2 Gas on Carbon Nanotubes. *J. Mater. Chem.* **2011**, *21*, 4502−4508.
(29) Ding, D. J.; Lou, X. W. SnO_2 Nanosheet Hollow Spheres with Improved Lithium Storage Capabilities. *Nanoscale* **2011**, *3*, 3586−3588.
(30) Cao, M. H.; Liu, T. F.; Gao, S.; Sun, G. B.; Wu, X. L.; Hu, C. W.; Wang, Z. L. Single Crystal Dendritic Micro-Pines of Magnetic α-Fe_2O_3: Large-Scale Synthesis, Formation Mechanism, and Properties. *Angew. Chem., Int. Ed.* **2005**, *44*, 4197−4201.
(31) Li, K. M.; Li, Y. J.; Lu, M. Y.; Kuo, C.; Chen, L. J. Direct Conversion of Single-Layer SnO Nanoplates to Multi-Layer SnO_2 Nanoplates with Enhanced Ethanol Sensing Properties. *Adv. Funct. Mater.* **2009**, *19*, 2453−2456.
(32) Yu, Q. X.; Zhu, J. H.; Xu, Z. Y.; Huang, X. T. Facile Synthesis of α-Fe_2O_3/SnO_2 Core-Shell Heterostructure Nanotubes for High Performance Gas Sensors. *Sens. Actuators, B* **2015**, *213*, 27−34.
(33) Niu, M. T.; Huang, F.; Cui, L. F.; Huang, P.; Yu, Y. L.; Wang, Y. S. Hydrothermal Synthesis, Structural Characteristics, and Enhanced Photocatalysis of SnO_2/α-Fe_2O_3 Semiconductor Nanoheterostructures. *ACS Nano* **2010**, *4*, 681−688.
(34) Wu, W.; Zhang, S. F.; Ren, F.; Xiao, X. H.; Zhou, J.; Jiang, C. Z. Controlled Synthesis of Magnetic Ion Oxides@SnO_2 Quasi-Hollow Core-Shell Heterostructures: Formation Mechanism, and Enhanced Photocatalytic Activity. *Nanoscale* **2011**, *3*, 4676−4684.
(35) Kang, J.; Kuang, Q.; Xie, Z. X.; Zheng, L. S. Fabrication of The SnO_2/α-Fe_2O_3 Hierarchical Heterostructure and Its Enhanced Photocatalytic Property. *J. Phys. Chem. C* **2011**, *115*, 7874−7879.
(36) Zhang, D. F.; Sun, L. D.; Jia, C. J.; Yan, Z. G.; You, L. P.; Yan, C. H. Hierarchical Assembly of SnO_2 Nanorod Arrays on α-Fe_2O_3 Nanotubes: A Case of Interfacial Lattice Compatibility. *J. Am. Chem. Soc.* **2005**, *127*, 13492−13493.
(37) Rumyantseva, M. N.; Kovalenko, V. V.; Gaskov, A. M.; Pagnier, T.; Machon, D.; Arbiol, J.; Morante, J. R. Nanocomposites SnO_2/Fe_2O_3: Wet Chemical Synthesis and Nanostructure Characterization. *Sens. Actuators, B* **2005**, *109*, 64−74.
(38) Wang, B.; Chen, J. S.; Lou, X. W. The Comparative Lithium Storage Properties of Urchin-Like Hematite Spheres: Hollow vs. Solid. *J. Mater. Chem.* **2012**, *22*, 9466−9468.
(39) Zhou, L.; Zhao, D. Y.; Lou, X. W. Double-Shelled $CoMn_2O_4$ Hollow Microcubes as Hgh-Capacity Anodes for Lithium Ion Batteries. *Adv. Mater.* **2012**, *24*, 745−748.
(40) Kim, H.-R.; Choi, K-II.; Kim, K.-M.; Kim, II-D.; Cao, G. Z.; Lee, J.-H. Ultra-Fast Responding and Recovering C_2H_5OH Sensors Using SnO_2 Hollow Spheres Prepared and Activated by Ni Templates. *Chem. Commun.* **2010**, *46*, 5061−5063.
(41) Zhang, D. F.; Sun, L. D.; Yin, J. L.; Yan, C. H. Low-Temperature Fabrication of Highly Crystalline SnO_2 Nanorods. *Adv. Mater.* **2003**, *15*, 1022−1025.
(42) Gu, X.; Chen, L.; Ju, Z. C.; Xu, H. Y.; Yang, J.; Qian, Y. T. Controlled Growth of Porous α-Fe_2O_3 Branches on β-MnO_2 Nanorods for Excellent Performance in Lithium-ion Batteries. *Adv. Funct. Mater.* **2013**, *23*, 4049−4056.
(43) Naisbitt, S. C.; Pratt, K. F. E.; Williams, D. E.; Parkin, I. P. A Microstructural Modle of Semiconducting Gas Sensor Response: The Effects of Sintering Temperature on The Response of Chromium (CTO) to Carbon Monoxide. *Sens. Actuators, B* **2006**, *114*, 969−977.
(44) Jinkawa, T.; Sakai, G.; Tamaki, J.; Miura, N.; Yamazoe, N. Relationship Between Ethanol Gas Sensitivity and Surface Catalytic Property of Tin Oxide Sensors Modified with Acidic or Basic Oxides. *J. Mol. Catal. A: Chem.* **2000**, *155*, 193−200.
(45) Kotsikau, D.; Ivanovskaya, M.; Orlik, D.; Falasioni, M. Gas-Sensitive Properties of Thin and Thick Film Sensors Based on Fe_2O_3-SnO_2 Nanocomposites. *Sens. Actuators, B* **2004**, *101*, 199−206.
(46) Neri, G.; Bonavita, A.; Micali, G.; Rizzo, G.; Pinna, N.; Niederberger, M.; Ba, J. Effect of The Chemical Composition on The Sensing Properties of In_2O_3-SnO_2 Nanoparticles Synthesized by a Non-Aqueous Method. *Sens. Actuators, B* **2008**, *130*, 222−230.
(47) Khoang, N. D.; Trung, D. D.; Duy, N. V.; Hoa, N. D.; Hieu, N. V. Design of SnO_2/ZnO Hierarchical Nanostructures for Enhanced Ethanol Gas-Sensing Performance. *Sens. Actuators, B* **2012**, *174*, 594−601.
(48) Ivanovskaya, M.; Kotsikau, D.; Faglia, G.; Nelli, P. Influence of Chemical Composition and Structural Factors of Fe_2O_3/In_2O_3 Sensors on Their Selectivity and Sensitivity to Ethanol. *Sens. Actuators, B* **2003**, *96*, 498−503.
(49) Weis, T.; Lipperheide, R.; Wille, U. Barrier-Controlled Carrier Transport in Microcrystalline Semiconducting Materials: Description with a Unified Model. *J. Appl. Phys.* **2002**, *92*, 1411−1418.
(50) Zhou, W. W.; Cheng, C. W.; Liu, J. P.; Tay, Y. Y.; Jiang, J.; Jia, X. T.; Zhang, J. X.; Gong, H.; Hng, H. H.; Yu, T.; Fan, H. J. Epitaxial Growth of Branched α-Fe_2O_3/SnO_2 Nano-Heterostructures with Improved Lithium-Ion Battery Performance. *Adv. Funct. Mater.* **2011**, *21*, 2439−2445.
(51) Gopal, R. C. B.; Cao, W.; Tan, O. K.; Zhu, W. Preparation of $Fe_2O_{3(0.9)}$-$SnO_{2(0.1)}$ by Hydrazine Method: Application as an Alcohol Sensor. *Sens. Actuators, B* **2002**, *81*, 170−175.
(52) Yin, L. W.; Li, M. S.; Bando, Y.; Golberg, D.; Yuan, X.; Sekiguchi, T. Tailoring The Optical Properties of Epitaxially Grown Biaxial ZnO/Ge, and Coaxial ZnO/Ge/ZnO and Ge/ZnO/Ge Heterostructures. *Adv. Funct. Mater.* **2007**, *17*, 270−276.
(53) Bao, M.; Chen, Y. J.; Li, F.; Ma, J. M.; Lv, T.; Tang, Y. J.; Chen, L. B.; Xu, Z.; Wang, T. H. Plate-like P-N Heterogeneous NiO/WO_3 Nanocomposites for High Performance Room Temperature NO_2 Sensors. *Nanoscale* **2014**, *6*, 4063−4066.
(54) Yamazoe, N.; Fuchigami, J.; Kishikawa, M.; Seiyama, T. Interations of Tin Oxide Surface with O_2, H_2O and H_2. *Surf. Sci.* **1979**, *86*, 335−344.
(55) Shimizu, Y.; Kuwano, N.; Hyodo, T.; Egashira, M. High H_2 Sensing Performance of Anodically Oxidized TiO_2 Film Contacted with Pd. *Sens. Actuators, B* **2002**, *83*, 195−201.

DOI: 10.1021/acsami.5b04751
ACS Appl. Mater. Interfaces 2015, 7, 19119−19125